https://doi.org/10.22226/2410-3535-2019-4-534-540 PACS: 430.30

Effect of treatment time on mechanical properties of pure copper processed by surface mechanical attrition treatment at cryogenic temperature

Jinxu Zhang, Hongjiang Pan, Hongliang Gao, Xu Yang, Xingfu Li, Xiaomin Liu, Baipo Shu, Cong Li, Yulan Gong, Xinkun Zhu†

†xk_zhu@hotmail.com

Faculty of Materials Science and Engineering, Kunming University of Science and Technology, Kunming, Yunnan, 650093, China

Bulk pure copper samples were subjected to surface mechanical attrition treatment (SMAT) at cryogenic temperature (liquid nitrogen environment) to obtain a gradient structure (GS) composed of GS layers on both sides and a coarse-grained (CG) layer in the core, with grain sizes varied from hundreds of nanometers to several micrometers. The grain sizes increased but the measured hardness decreased along the depth of the gradient-grained Cu samples. The GS samples exhibited high yield strength (YS) while the uniform elongation (UE) showed only a slight reduction in tensile testing. The high strength and superior UE in the GS samples were believed to be associated with the mechanical incompatibility and interaction between the GS and CG layers. Variation of SMAT processing time could obtain GS layers with different volume fractions and therefore resulting in a different mechanical performance of GS Cu samples. Thus, there was an optimal SMAT processing time associating with the volume fractions of the GS layers, which provided an excellent combination in strength and UE of the GS Cu sample. The loading-unloading-reloading (LUR) tests indicated that higher hetero-deformation induced (HDI) stress could be obtained at a longer SMAT processing time. The HDI stress is caused by hetero deformation among different layers, which increased with increasing SMAT processing time.

Keywords: surface mechanical attrition treatment, gradient structure, mechanical properties, HDI stress, geometrically necessary dislocations.

1. Introduction

The conventional metallic materials invariably display the trade-off between the strength and ductility, consequently limit the practical application of materials in the engineering field [1, 2]. There is however a relentless quest to reach a more superior combination of strength and ductility. Recently, a GS material ubiquitously exist in natural materials such as bone, shells, and trees and now increasingly adopt in engineering systems to achieve desirable combinations of high strength and excellent ductility [3 – 7].

Efforts have been devoted to developing substantial strategies for improving the ductility and strength simultaneously of materials in recent years. The severe plastic deformation (SPD) techniques have been extensively investigated to produce ultrafine-grained (UFG) (<1 μm) or nanocrystalline (NC) materials (<100 nm) over several decades [8, 9], which could significantly improve the YS but obtain the inadequate ductility [10]. Therefore, a primary challenge is to design novel microstructures to restore a respectable ductility of these high-strength metals to achieve the desired strength-ductility synergy [11].

Lu et al. [12] synthesized a high density of nanotwins (NT) in pure copper samples and the strength about 10 times higher than that of coarse grained copper and a high elongation-to-failure value of 13.5%. The interaction between twin boundaries and dislocations is the main cause of high strain hardening [13]. Wang et al. [14] prepared a Cu sample with a bimodal grain sizes distribution, which leaded to a high tensile ductility — 30% uniform elongation. By introducing high density of second-phase particles, pre-existing deformation twins, deformation twinning and increasing the ratio of high-angle grain boundaries (HAGBs) [15], Zhao et al [16]. simultaneously improved the strength and ductility of samples.

Numerous strengthening mechanisms in metals have drawn increasing attention in recent years, including strain gradient [17], multiaxial stress state, HDI strengthening and HDI hardening [18], which have been proposed to elucidate the intrinsic effects associated with the strain gradient.

Recently, surface nanocrystallization (SNC) technology has been generally considered as a new method to improve the global mechanical properties of the materials by optimizing the surface structure [19]. Thus, a GS sample can be produced by SMAT process, in which the grain sizes vary from hundreds of nanometers to several micrometers along the depth of surface layer. The GS can effectively restrain the strain localization, thereby improved the mechanical properties of metallic materials.

In this work, the GS pure Cu was prepared by SMAT process, which consisted of the CG layer in the core and the GS surface layer on both sides. The loading-unloading-reloading

tests, microstructure and geometrically necessary dislocations (GNDs) analyses were carried out to estimate the effects of treatment time on mechanical properties of GS pure Cu. The results may be instructive on obtaining high strength and superior ductility in GS materials.

2. Experimental details

A commercially pure copper (99.995 wt.% purity) was cut into plates with dimensions of 5×80×100 mm^3. Then the plates were annealed in vacuum at 923 K for 2 h to obtain homogeneous coarse-grained (CG) structure, and the samples were polished to a mirror finish prior to SMAT processing. Subsequently, 208 stainless steel balls with diameter of 8 mm were used in SMAT processing with a vibration frequency of 50 Hz. Both sides of the annealed Cu were subjected to SMAT treatment in cylinder-shaped chamber at 77 K (liquid nitrogen environment) for 10 min, 30 min and 60 min to obtain a GS, respectively. Briefly, a large number of balls impacted the sample surface repeatedly from various directions, leading to strain induced grain refinement at the surface. For simplicity, such samples with GS were called SMAT-processed samples.

The all tensile samples were cut into dog-bone-shaped with a gauge length of 15 mm, a width of 5 mm and a thickness of 5 ± 0.1 mm by wire-electrode cutting. Standard uniaxial tensile tests were carried out on a SHIMADZU Universal Tester at room temperature and at a strain rate of 5.0×10^{-4} s^{-1}. The loading-unloading-reloading tests were carried out at 15 varying applied strains to evaluate HDI stress. The stress measured by the LUR tests was used to be called back stress [20], but it was found recently that HDI stress is a more accurate term [18]. In the present work, the strains of loading-unloading-reloading tests were set as1%, 2%, 3%, 4%, 5%, 6%, 7%, 8%, 9%, 10%, 11%, 12%, 13%, 14%, and 15%, respectively. At each applied strain, the sample was first unloaded with the unloading rate of 500 N · min^{-1} to 20 N, and then was reloaded with the strain rate of 5.0×10^{-4} s^{-1} to the next applied strain. Three samples were tested at each condition to ensure good repeatability of the results. The tensile properties of annealed and SMAT-processed samples were listed in Table 1.

The hardness profile along the depth of SMAT-processed and annealed samples was measured by using a Vickers hardness tester with a load of 0.49 N and a dwell time of 15 s. Final results were determined by averaging the values of 5 indentation measurements. Also, the distance between adjacent indentations was 20 μm to exclude the interaction of two neighboring indent and the total test depth from the SMAT-processed surface to the core was about 500 μm.

The microstructures of SMAT-processed samples were observed on a high-resolution field emission Carl Zeiss-Auriga-45-66 scanning electron microscope (SEM) equipped with a fully automatic Oxford Instruments Aztec 2.0 EBSD system (channel 5 software). The distribution and statistics of GNDs were evaluated using EBSD images by the channel 5 software.

3. Results and discussion

Fig. 1a shows the variations of hardness with the depth from the topmost surface of the SMAT-processed and annealed samples. The schematic diagram of the combination for the hardness curves and metallographic micrograph of the SMAT-10 min Cu sample are shown in Fig. 1b. The red and green curves represent the hardness curves for the annealed and SMAT-10 min samples, respectively. Two blue dotted lines are used to represent the thickness of the GS layer of SMAT-10 min sample, and the thickness is approximately 350 μm.

It can be seen from Fig. 1a that the hardness of the annealed sample is approximately 0.60 GPa, and is provided as a reference. However, the hardness values of GS samples gradually decreased with depth, and began to level-off at the depth of 300 μm. The hardness was also affected by the SMAT treating time as shown in Fig. 1a. At the same depth, the hardness was higher in the sample SMAT-treated for a longer period. For example, the highest hardness value was ~1.24 GPa and detected at the topmost surface of the SMAT-60 min sample.

For convenience, we defined the top surface layer as the ultrafine-grained (UFG) layer. The whole GS layer included the UFG layer and the deformed CG layer with the grain sizes changing from hundreds of nanometers to several micrometers [21]. The hardness values of the SMAT-processed samples gradually decrease with increasing depth from the surface and eventually stabilize. This could be attributed to the samples surface subjected to the largest strain and the highest strain rate during the SMAT treatment, and the surface grain refinement was the most severe.

The plastic strain and strain rate of the deformed layer farther away from the surface layer are gradually reduced, i. e., the topmost surface layer is carried to the largest strains and strain rates, which results in hardness curves show a gradient change [22]. In addition, this performance can also be explained by the metallographic micrograph in Fig. 1b, which shows that the grain sizes increase significantly with an increase of depth from the SMAT-processed surface to the core. When the hardness curve of SMAT-10 min sample is reduced to the lowest position, the thickness remains basically the same as that of GS layer. By comparing the GS samples with different treatment times, it can be clearly observed

Table 1. Details of samples and tensile properties of annealed and SMAT-processed samples.

Samples	Yield strength (YS) ($\sigma_{0.2\%}$), MPa	Uniform elongation (UE), %	Ultimate tensile strength (UTS), MPa
Cu-annealed	67.1± 5	38.3 ± 0.3	210.7 ± 5
Cu-SMAT-10 min	197.4 ± 5	22.9 ± 0.7	224.4 ± 5
Cu-SMAT-30 min	208.7 ± 5	16.5 ± 0.4	234.5 ± 6
Cu-SMAT-60 min	217 ±12	1.73 ± 0.5	233.7 ±10

that higher surface hardness value and thicker GS layer were obtained after longer SMAT processing time. However, the hardness value of surface and the thickness of GS layer in SMAT-60 min sample do not significantly improve comparing with the ones of SMAT-30 min, which indicates that there is a limit value of strengthening for pure Cu samples treated by SMAT process at cryogenic temperature (liquid nitrogen environment).

Fig. 2a shows the engineering stress-strain curves of the SMAT-processed and the annealed samples, and the SMAT processing time was 10 min, 30 min, and 60 min, respectively. With the increase of SMAT processing time, the YS (0.2% offset) obviously increases while the UE slightly decreases. From Table 1, we can observe YS of 197.4 ± 5 MPa (SMAT-10 min), 208.7 ± 5 MPa (SMAT-30 min), and 217 ± 12 MPa (SMAT-60 min), respectively. The YS of all SMAT-processed Cu samples is nearly three times value of the annealed sample (67.1 ± 5 MPa). The SMAT-processed samples exhibit a UE of 22.9 ± 0.7 (SMAT-10 min), 16.5 ± 0.4 (SMAT-30 min) and 1.73 ± 0.5 (SMAT-60 min). Some investigations have indicated that stand alone GS layer always exhibits poor UE, but our SMAT-processed samples show excellent UE. According to the deformation behavior of heterogeneous materials [20], the CG matrix has effectively suppressed the early-emerging strain localization and failure of GS layer during the tension [23, 24]. In this work, the GS pure Cu samples are composed of a GS layer and a CG matrix, and the GS layers provide the improvement of the sample strength, while the CG matrix ensures the plasticity of the sample. Consequently, we obtain a superior combination of UE and strength in the GS samples that is not accessible to conventional homogeneous microstructures [20, 24, 25]. The SMAT-10 min sample shows the best combination in strength and UE. However, comparing with the SMAT-30 min sample, the UE of SMAT-60 min sample drop rapidly, although the YS is slightly improved. This indicates that there is a limit value of strengthening for pure Cu samples treated by SMAT process at cryogenic

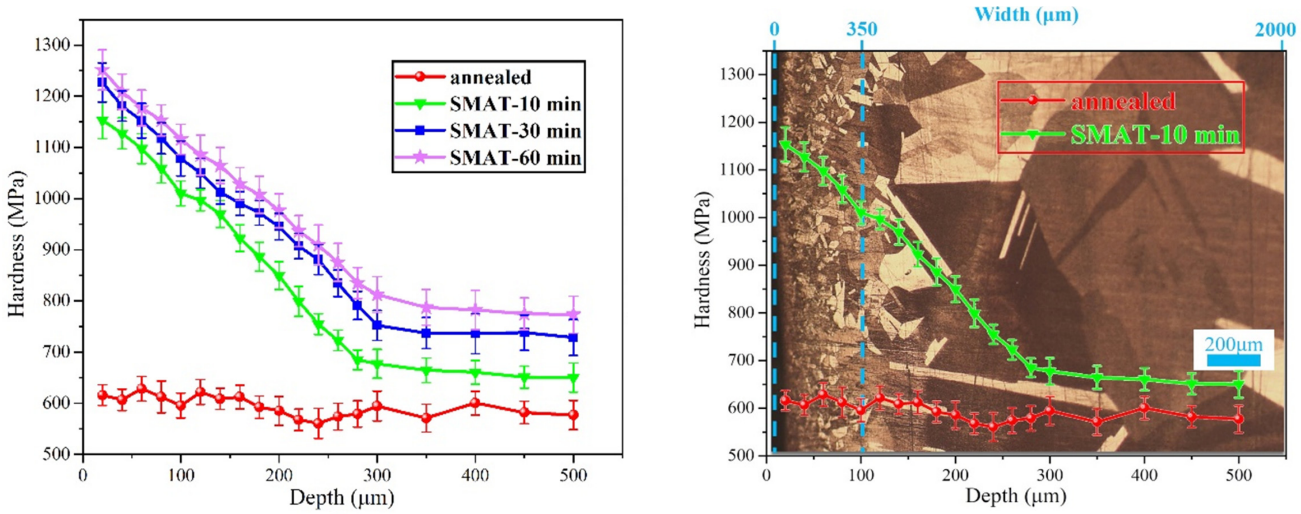

Fig. 1. (Color online) Variation in hardness as a function of depth from the surface in the annealed and SMAT-processed samples, SMAT processing time was 5 min, 15 min, and 30 min, respectively (a), schematic diagram of the combination for the hardness curves and metallographic micrograph of the SMAT-10 min Cu sample (b).

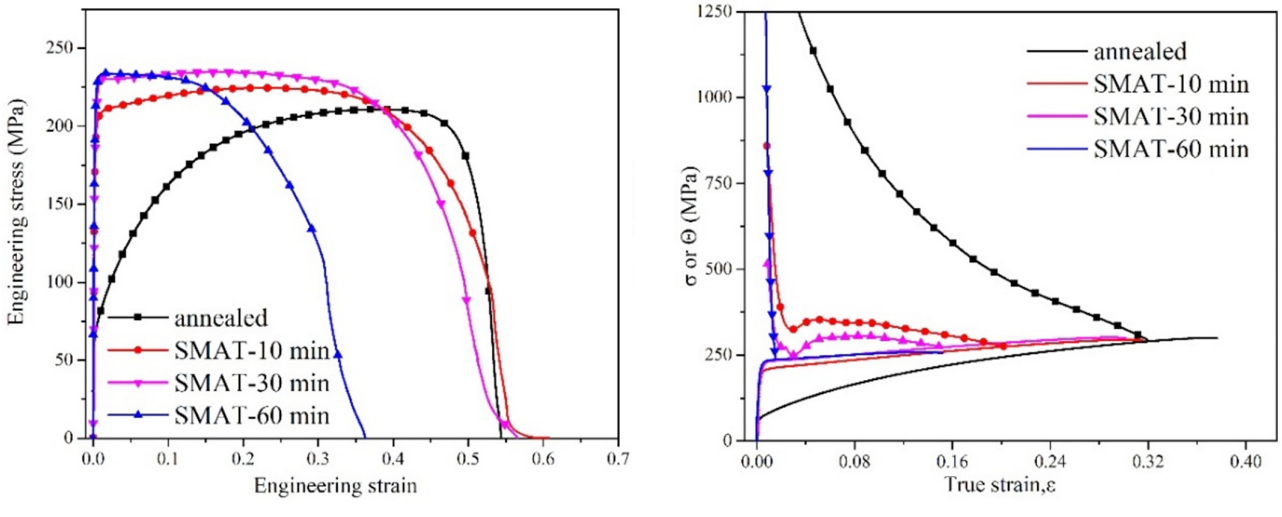

Fig. 2. (Color online) Engineering stress-strain curves of annealed and SMAT-processed samples (a); true stress-strain curves and strain hardening rate curves of annealed and SMAT-processed samples (b).

temperature (liquid nitrogen environment), which is also consistent with the variation of hardness curves, as shown in Fig. 1. Hereby, we define the value of YS × UE to estimate the comprehensive mechanical properties of the SMAT-processed samples, i.e., an excellent comprehensive mechanical properties can be obtained corresponding to a higher value of YS × UE. The value of SMAT-10 min sample is 4520.46, the value of SMAT-30 min sample is 3443.55, and the value of SMAT-60 min sample is 375.41. Therefore, it can be concluded that the best comprehensive mechanical properties can be obtained in the SMAT-10 min sample, which indicates that an optimal GS layer volume fraction can be obtained for a SMAT-10 min treatment in the bulk samples. This results in an excellent combination in strength and YS of the GS samples.

Fig. 2 b shows the strain hardening rate ($\Theta = d\sigma/d\varepsilon$, where σ is the true stress and the ε is the true strain) as a function of true strain, and it is an important indicator to evaluate the UE of metallic materials. The intersection of true stress and strain-hardening rate curves represents the onset of localized deformation, i.e., the necking point. It is evident from Fig. 2 b that $\varepsilon_{u\ annealed} > \varepsilon_{u\ SMAT\text{-}10\ min} > \varepsilon_{u\ SMAT\text{-}30\ min} > \varepsilon_{u\ SMAT\text{-}60min}$. For all SMAT-processed samples, the strain hardening rate sharply reduces in the elastic-plastic transition stage (true strain is less than 2%). However, in the plastic deformation stage (true strain is larger than 2%), the SMAT-processed samples show a slower strain hardening rate reduction than that of the CG samples. It is remarkable in the SMAT-processed samples that the strain hardening rate has a slight up-turn characteristic, especially for the SMAT-10 min and SMAT-30 min samples. This phenomenon is described in recent report of GS IF steel structures [24].

Fig. 3 a shows the loading-unloading-reloading stress-strain curves of annealed and SMAT-processed samples. It can be seen that the hysteresis loop becomes larger with the SMAT processing time increases, which indicate that a larger HDI stress in the GS samples, as shown in Fig. 3 b. The HDI stress is caused by hetero-deformation among different layers. The softer layer will be subjected to higher plastic strain with increasing tensile strain, which create a strain gradient that needs to be accommodated by geometrically necessary dislocations (GNDs) in the softer layer. GNDs produce back stress in the soft layer (domain) and forward stress in the hard layer (domain), which together produces the HDI stress measured by the LUR tests [18]. On the contrary, the annealed samples with homogeneous coarse grains show a smaller hysteresis loop and the HDI stress in annealed Cu sample is low.

The cross-sectional EBSD images in near the surfaces of SMAT-processed samples are obtained via SEM-EBSD. The red lines and black lines represent low-angle grain boundaries (LAGBs) ($2° \le \theta < 15°$) and high-angle grain boundaries (HAGBs) ($\theta > 15°$), respectively. The above is obtained by analysis using Channel 5 software [26]. The results are shown in Fig. 4. The scan size was 10 × 9 μm (Fig. 3 a) and 6.6 × 6.6 μm (Fig. 4 b, d), respectively, and the step size was set as 40 nm.

Fig. 4 displays that the crystal grains in the surface of both in SMAT-30 min and SMAT-60 min samples are severely refined, but the SMAT-60 min sample shows a better performance in refinement. Additionally, the number of LAGBs is apparent higher than that of HAGBs for both SMAT-processed samples. It indicates that an apparent crystal grains refinement can be obtained at the longer SMAT processing time.

Additionally, this phenomenon corresponding to that shows in the hardness curves in Fig. 1, i.e., a higher hardness value is from the finer crystal grains of the treatment surface, which increased with the increasing SMAT processing time. However, the hardness decreased significantly with an increase of depth from the SMAT-processed surface to the core.

Fig. 5 a, c represent the GNDs distribution images of SMAT-60 min and SMAT-30 min sample obtained from EBSD results by using Channel 5 software [26]. The histograms of GNDs density distribution are shown in Fig. 5 b, d calculated from the EBSD results in Fig. 4. It is evident from the Fig. 5 that the density of GNDs in SMAT-60 min sample (ρ_{GND} (mean = 215.68735)) is obvious higher than that of SMAT-30 min sample

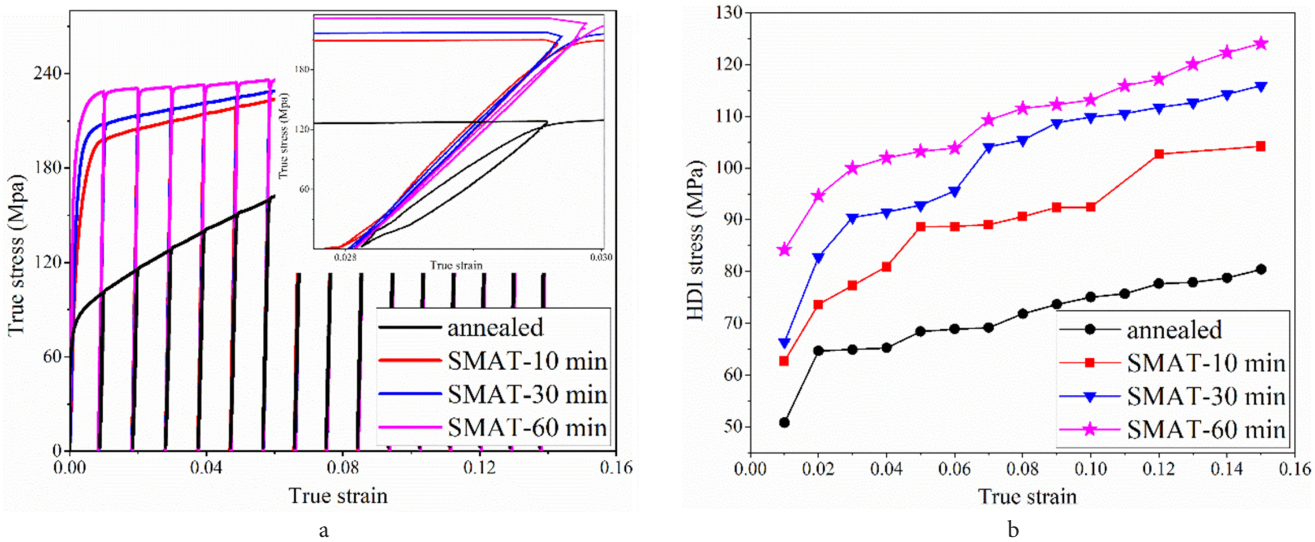

Fig. 3. (Color online) Loading-unloading-reloading stress-strain curves of annealed (CG) and SMAT-processed (GS) samples and the inset was magnified view of the third hysteresis loop (a). Evolution of HDI stress with increasing applied strain (b).

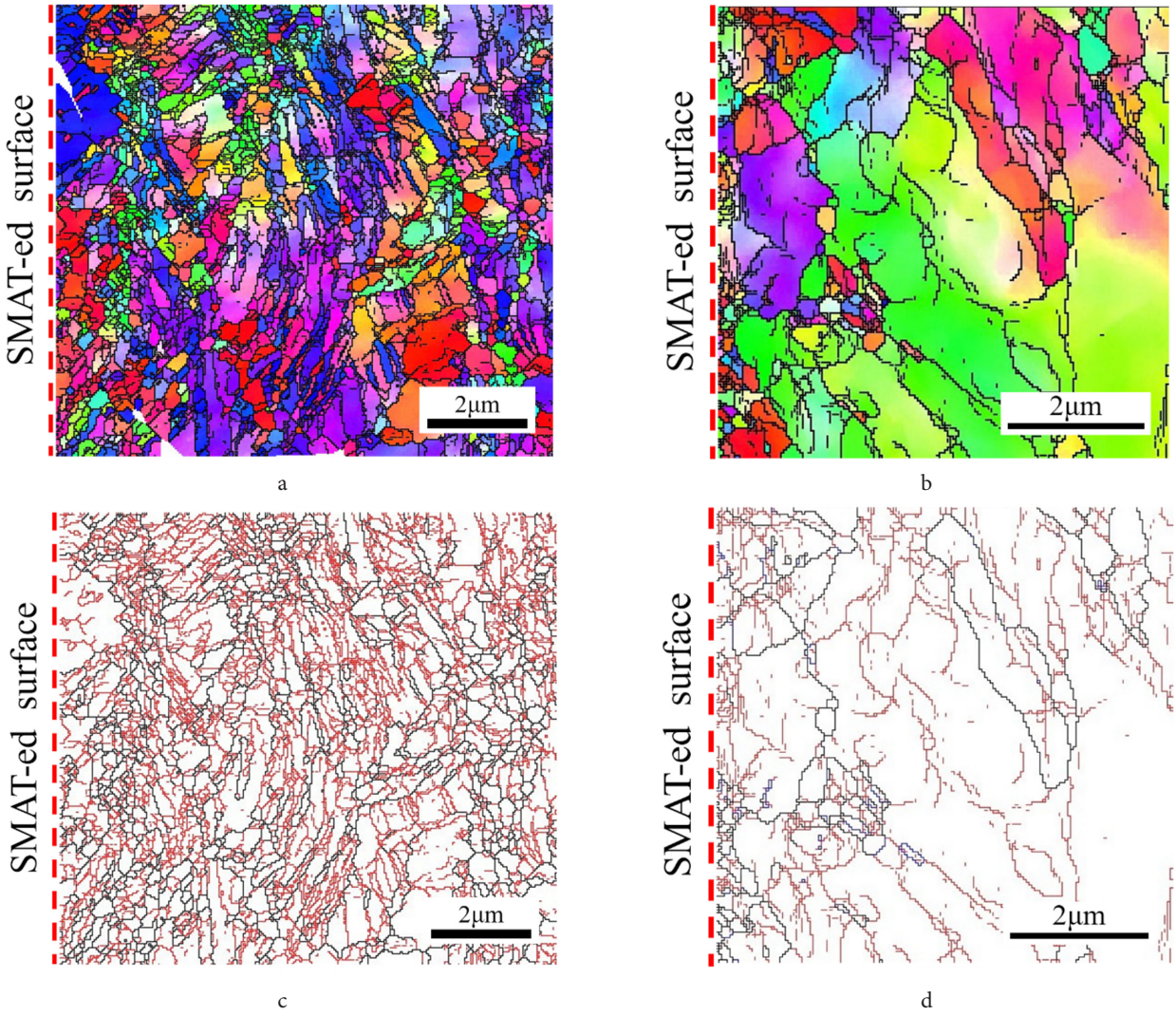

Fig. 4. (Color online) The cross-sectional EBSD images in near the surfaces of SMAT-processed samples. SMAT-60 min (a, c), SMAT-30 min (b, d). (Orientation map (a, b); boundary misorientation map (c, d). The red lines and black lines represent low-angle grain boundaries (LAGBs) ($2° \le \theta < 15°$), high-angle grain boundaries (HAGBs) ($\theta > 15°$), respectively).

(ρ_{GND} (mean = 236.99523)), which indicates that the longer the SMAT processing time, the higher the GND density.

The GNDs represented an additional storage of dislocations demanded to accommodate the lattice curvature that occurred whenever there was an inhomogeneous plastic deformation [27]. The GNDs could be obtained directly from EBSD data based on kernel average misorientation (KAM), and the grain boundary misorientation of GNDs density was drawn from 0 to 2°. The GNDs density could be evaluated by the strain gradient model established by Gao and Kubin [28, 29]:

$$\rho_{GND} = \frac{2\theta}{\mu b}$$

where μ is the unit length (step size), b is the Burgers vector ($b = 0.256$ nm), and θ is the local misorientation (from 0 to 2°).

In this work, the GS samples produced by SMAT process consisted of the CG layer in the core and the GS surface layer on the both sides. During tensile testing, the soft CG in the core began to deform first but it needed to deform together with the neighboring GS layer. Therefore, the CG layer cannot plastically deform freely. Resulting in an apparent mechanical incompatibilities was produced between GS and CG layers, which needed to be accommodated by the GNDs to maintain continuity [25]. Consequently, there would be a plastic strain gradient in the GS/CG architecture, and which induced an extra HDI strengthening [18, 30]. The HDI stress would lead to a synergetic strengthening to increase the global measured YS of the GS material [18, 20, 31].

The GS/CG layers sustained different plastic strains with the increasing loading strain, and strain gradients were expected to exist near the domain boundaries in both. The effect of HDI stress increased with increasing SMAT processing time due to the increasing structural gradient [32]. Consequently, the HDI hardening would be induced with increasing strain gradient. The HDI hardening would help with preventing necking during tensile testing therefore improving UE of GS materials [18, 20, 33, 34].

As shown in Fig. 6, the YS and UE of the conventional techniques are mainly distributed below the red curve. The data shows in the red circle represent SMAT-processed Cu samples, which are from this work and reference [36], respectively. Obviously, in our study, the SMAT-processed Cu samples display a superior combination in YS and UE compared to other literature values.

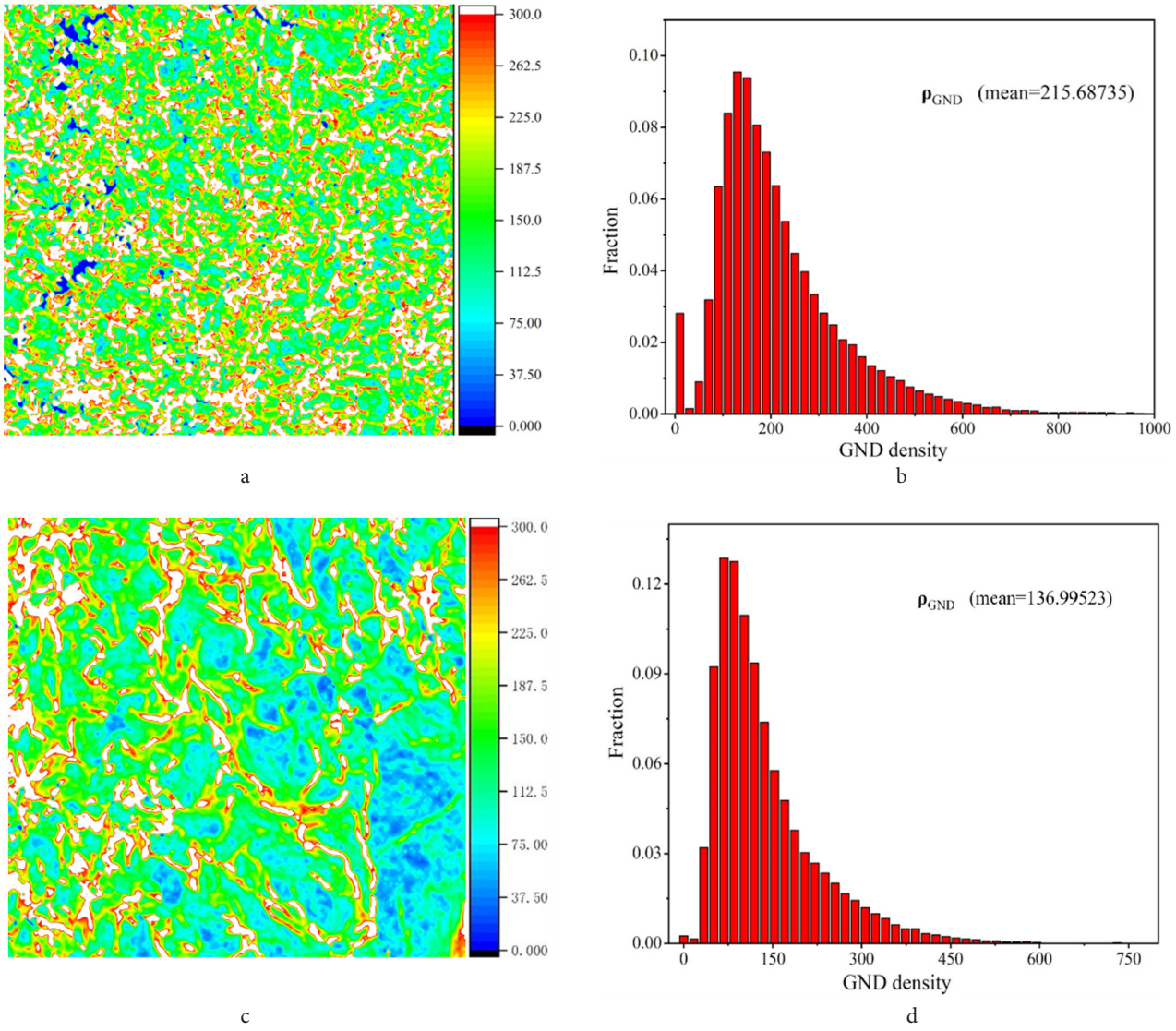

Fig. 5. (Color online) GNDs distribution images and GNDs density distribution histograms of SMAT-processed samples, respectively. SMAT-60 min (a, b), SMAT-30 min (c, d).

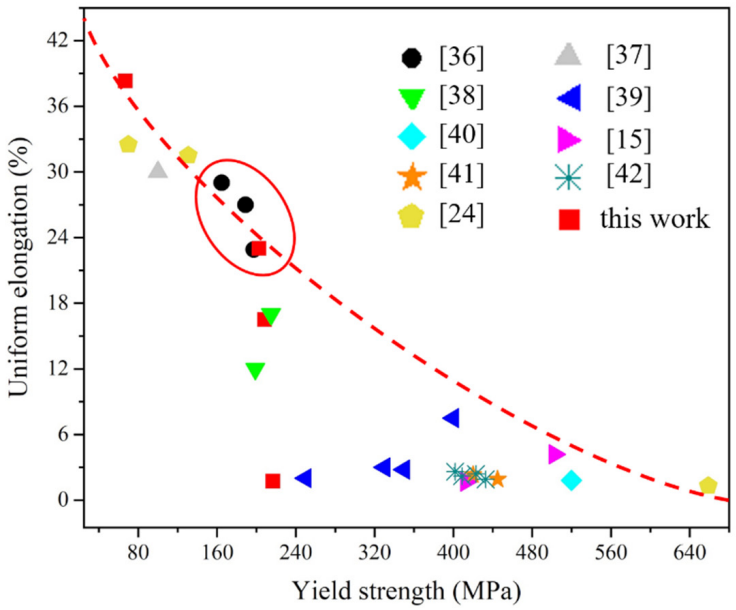

Fig. 6. (Color online) Comparing the tensile properties of pure copper samples processed by different processes. These are the data from this work and available literature data.

4. Conclusions

In conclusion, the GS pure copper samples produced by SMAT process showed CG layer in the core and GS surface layer on both sides. The SMAT-10 min samples showed a threefold improvement in the YS while the UE showed only a slight decrease compared with annealed sample. An optimal volume fraction of GS layers could be obtained in the bulk samples after SMAT-10 min treatment, resulting in an excellent combination of YS and UE of the GS samples. Therefore, there was a limit value of strengthening for pure Cu samples treated by SMAT process at cryogenic temperature (liquid nitrogen environment). By controlling the volume fractions of GS layers, it was possible to improve the strength and UE simultaneously to achieve the excellent mechanical properties.

The high strength and superior UE in the GS samples were believed to be associated with the mechanical incompatibility and interaction between the GS and CG layers. An apparent HDI stress were observed in the GS Cu samples, which could be attributed to the accumulation of a large amount of GNDs.

Acknowledgments. Special thanks to Prof. Yuntian Zhu, who made instructive comments and recommendations on the research direction of this paper. The authors also would like to acknowledge financial support by the National Natural Science Foundation of China (NSFC) under Grant No. 51561015, No. 51664033 and No. 51861013.

References

1. N. Tsuji, Y. Ito, Y. Saito, Y. Minamino. Scripta Materialia. 47, 893 (2002). Crossref
2. Y. Wei, Y. Li, L. Zhu, Y. Liu, X. Lei, G. Wang, Y. Wu, Z. Mi, J. Liu, H. Wang. Nature Communications. 5, 3580 (2014). Crossref
3. M. A. Meyers, P. Y. Chen, Y. M. Lin, Y. Seki. Progress in Materials Science. 53, 1 (2008). Crossref
4. H. D. Espinosa, J. E. Rim, F. Barthelat, M. J. Buehler. Progress in Materials Science. 54, 1059 (2009). Crossref
5. K. Ghavami. Cement & Concrete Composites. 27, 637 (2005). Crossref
6. H. Kou, J. Lu, Y. Li. Advanced Materials. 26, 5518 (2014). Crossref
7. K. Lu. Science. 345, 1455 (2014). Crossref
8. Y. Estrin. Acta Materialia. 61, 782 (2013). Crossref
9. D. A. Hughes, N. Hansen. Acta Materialia. 48, 2985 (2000). Crossref
10. A. P. Zhilyaev, T. G. Langdon. Prog.mater.sci. 53, 893 (2008). Crossref
11. E. Ma, T. Zhu. Materials Today. 20 (6), 323 (2017). Crossref
12. K. Lu, L. Lu, S. Suresh. Science. 324, 349 (2009). Crossref
13. L. Lu, Y. Shen, X. Chen, L. Qian, K. Lu. Science. 304, 422 (2004). Crossref
14. Y. Wang, M. Chen, F. Zhou, E. Ma. Nature. 419, 912 (2002). Crossref
15. Y. H. Zhao, J. F. Bingert, X. Z. Liao, B. Z. Cui, K. Han, A. V. Sergueeva, A. K. Mukherjee, R. Z. Valiev, T. G. Langdon, Y. T. Zhu. Advanced Materials. 18, 2949 (2010). Crossref
16. Y. H. Zhao, X. Z. Liao, S. Cheng, E. Ma, Y. T. Zhu. Advanced Materials. 18, 2280 (2010). Crossref
17. S. S. Chakravarthy, W. A. Curtin. Proc. Natl. Acad. Sci. U. S. A. 108, 15716 (2011). Crossref
18. Y. Zhu, X. Wu. Mater. Res. Lett. 7, 393 (2019).
19. P.L. Orsetti Rossi, M. Sellars. Journal of Materials Science & Technology. 15, 193 (1999). Crossref
20. X. L. Wu, Y. T. Zhu. Mater. Res. Lett. 5, 527 (2017). Crossref
21. X. Huang. Science. 312, 249 (2006). Crossref
22. K. Wang, N. R. Tao, G. Liu, J. Lu, K. Lu. Acta Materialia. 54, 5281 (2006). Crossref
23. T. H. Fang, W. L. Li, N. R. Tao, K. Lu. Science. 331, 1587 (2011). Crossref
24. X. Wu, P. Jiang, L. Chen, F. Yuan, Y. T. Zhu. Proc. Natl. Acad. Sci. U. S. A. 111, 7197 (2014). Crossref
25. X. L. Wu, M. X. Yang, F. P. Yuan, G. L. Wu, Y. J. Wei, X. X. Huang, Y. T. Zhu. Proc. Natl. Acad. Sci. U. S. A. 112, 14501 (2015). Crossref
26. H. J. Yang, S. M. Yin, C. X. Huang, Z. F. Zhang, S. D. Wu, S. X. Li, Y. D. Liu. Advanced Engineering Materials. 10, 955 (2010). Crossref
27. H. J. Gao, Y. G. Huang. Scripta Materialia. 48, 113 (2003). Crossref
28. M. Calcagnotto, D. Ponge, E. Demir, D. Raabe. Materials Science And Engineering a-Structural Materials Properties Microstructure And Processing. 527, 2738 (2010). Crossref
29. H. Gao, Y. Huang, W. D. Nix, W. J. Hutchinson. Journal of the Mechanics & Physics of Solids. 47, 1239 (1999). Crossref
30. M. X. Yang, Y. Pan, F. P. Yuan, Y. T. Zhu, X. L. Wu. Mater. Res. Lett. 4, 145 (2016).
31. X. L. Wu, P. Jiang, L. Chen, J. F. Zhang, F. P. Yuan, Y. T. Zhu. Mater. Res. Lett. 2, 185 (2014). Crossref
32. X. Hu, S. Jin, Z. Hao, Y. Zhe, Y. Jian, Y. Gong, Y. Zhu, S. Gang, X. Zhu. Metallurgical & Materials Transactions A. 48, 1 (2017).
33. K. Park, M. Nishiyama, N. Nakada, T. Tsuchiyama, S. Takaki. Materials Science & Engineering A. 604, 135 (2014). Crossref
34. M. X. Yang, F. P. Yuan, Q. G. Xie, Y. D. Wang, E. Ma, X. L. Wu. Acta Materialia. 109, 213 (2016). Crossref